

Efficient Neural Controlled Differential Equations via Attentive Kernel Smoothing

Egor Serov¹ Ilya Kuleshov¹ Alexey Zaytsev¹

Abstract

Neural Controlled Differential Equations (Neural CDEs) provide a powerful continuous-time framework for sequence modeling, yet the roughness of the driving control path often restricts their efficiency. Standard splines introduce high-frequency variations that force adaptive solvers to take excessively small steps, driving up the Number of Function Evaluations (NFE). We propose a novel approach to Neural CDE path construction that replaces exact interpolation with Kernel and Gaussian Process (GP) smoothing, enabling explicit control over trajectory regularity. To recover details lost during smoothing, we propose an attention-based Multi-View CDE (MV-CDE) and its convolutional extension (MVC-CDE), which employ learnable queries to inform path reconstruction. This framework allows the model to distribute representational capacity across multiple trajectories, each capturing distinct temporal patterns. Empirical results demonstrate that our method, MVC-CDE with GP, achieves state-of-the-art accuracy while significantly reducing NFEs and total inference time compared to spline-based baselines.

1. Introduction

Sequential data processing is a fundamental challenge across a wide range of disciplines, including the analysis of medical records (Harutyunyan et al., 2017), financial dynamics (Zhang et al., 2018), and physical systems (Raissi et al., 2019). Most neural architectures for sequential data implicitly assume that observations lie on a regular temporal grid, enabling the direct application of discrete-time models such as recurrent or convolutional networks. However, this assumption is frequently violated in real-world settings. Sensor failures, asynchronous measurements, and missing data often result in irregularly sampled time series.

¹Applied AI Institute. Correspondence to: Egor Serov <e.serov@applied-ai.ru>.

A more rigorous approach is to treat the latent state evolution as a continuous-time process. This paradigm shift gained traction with Neural ODEs (Chen et al., 2018), which model the dynamics of the hidden state via ordinary differential equations. However, standard Neural ODEs are determined by their initial state and do not naturally adjust to incoming observations over time. To address this, Neural Controlled Differential Equations (Neural CDEs) (Kidger et al., 2020) were introduced as a principled framework for processing irregularly observed sequences. Their central idea is to represent the input data as a continuous-time control signal $\mathbf{X}(t)$, obtained via interpolation, and to evolve a hidden state $\mathbf{z}(t)$ according to the controlled differential equation

$$\frac{d\mathbf{z}(t)}{dt} = f_\theta(\mathbf{z}) \frac{d\mathbf{X}(t)}{dt}. \quad (1)$$

where the vector field f_θ is parameterized by a neural network. This formulation allows Neural CDEs to naturally handle missing values and irregular sampling while maintaining a continuous-time latent representation.

The computational cost of Neural CDEs is dominated by the numerical integration of this equation. In particular, it is closely tied to the number of times the solver evaluates the vector field function f_θ , commonly referred to as the NFE. Modern implementations typically rely on adaptive-step solvers, which aim to minimize NFE while satisfying a prescribed error tolerance by taking larger steps in regions where the dynamics are smooth.

However, there is a direct trade-off: NFE is highly sensitive to the regularity of the input trajectory. In practice, real-world time series are often noisy, and accurate interpolations of such data can produce highly irregular or jagged paths. This forces adaptive solvers to take many small integration steps, dramatically increasing NFE and computational cost. As a consequence, Neural CDEs can be an order of magnitude slower than more traditional time-series modeling approaches, limiting their practical applicability.

In this work, we propose replacing precise interpolation schemes with smoothing-based alternatives, thereby substantially reducing trajectory irregularity and accelerating numerical integration by up to an order of magnitude, without sacrificing predictive performance. To mitigate the po-

tential loss of high-frequency information caused by over-smoothing, we introduce an attention-based architecture inspired by Q-Former models (Li et al., 2023a). This mechanism adaptively aggregates information from multiple smoothed versions of the input, each capturing different temporal scales or regions of the sequence.

Conceptually, our approach can be viewed as a novel form of temporal parallelization for Neural CDEs: rather than integrating a single high-fidelity trajectory, we distribute interpolation precision across several smoother Neural CDE paths and learn to recombine them. This yields significant computational savings while preserving the expressive power of the continuous-time model.

Our main contributions are as follows:

- We identify stiffness as a primary driver of the high NFE in Neural CDEs, and empirically demonstrate that accurate interpolations of noisy real-world data can severely degrade solver efficiency.
- We propose replacing precise interpolation schemes with smoothing-based Kernel and GP alternatives for Neural CDEs. Such smoothing significantly reduces trajectory roughness and accelerates numerical integration by up to an order of magnitude.
- To counteract information loss induced by over-smoothing, we introduce an attention-based architecture inspired by Q-Former models named Multi-View Controlled Differential Equations (MV-CDE) and its convolutional extension, MVC-CDE. They adaptively aggregate information from multiple smoothed versions of the input, each capturing different temporal regions or scales.
- We reinterpret our method as a form of temporal parallelization for Neural CDEs, distributing interpolation precision across several smoother continuous-time trajectories and learning to recombine them into a single expressive representation.
- We validate our approach on real-world benchmarks. Our method achieves state-of-the-art accuracy while demonstrating speedups of $4.3\times$ to $14.5\times$ over standard Neural CDEs, along with superior robustness to additive noise.

2. Related Work

Neural Controlled Differential Equations. Neural ODEs (Chen et al., 2018) introduced continuous-depth modeling, yet their dependence on fixed initial conditions limits them to tabular data or requires hybrid discrete-continuous updates like ODE-RNNs (Rubanova et al., 2019). To address this, Kidger et al. (2020) formulated Neural CDEs, in

which the dynamics are driven by a continuous control path interpolated from observations. While this architecture effectively generalizes Recurrent Neural Networks (Oh et al., 2025) to irregular time series, a fundamental limitation remains: the computational cost is intrinsically tied to the regularity of the trajectory. Regardless of the learned vector field, the solver must traverse the geometric complexity of the driving path.

Interpolation and Path Regularity. Significant efforts have focused on regularizing the latent dynamics to reduce NFEs, employing penalties on higher-order derivatives (Kelly et al., 2020), optimal transport (Finlay et al., 2020), or stochastic end-time regularization (Ghosh et al., 2020). However, since Neural CDE dynamics are multiplicative, the solver step size is still determined by the roughness of the driving control path. Standard exact interpolation schemes force the path through every noisy observation, resulting in high-frequency variations and large derivatives (de Boor, 1978; Reinsch, 1967). As the local truncation error scales with these derivatives (Hairer et al., 1993), adaptive solvers must drastically reduce step sizes to maintain accuracy (Dormand & Prince, 1980; Morrill et al., 2022). Unlike prior work confined to deterministic interpolants, we propose explicit path smoothing via non-parametric kernels (Wand & Jones, 1995) or Heteroscedastic Gaussian Processes (Rasmussen & Williams, 2006) to decouple integration cost from input noise.

Stochastic and Probabilistic Approaches. Incorporating uncertainty directly into differential equations, Neural SDEs (Li et al., 2020; Kidger et al., 2021b) extend the CDE framework with diffusion terms. While powerful, this necessitates complex stochastic integrators like Euler-Maruyama (Kloeden & Pearson, 1977), significantly increasing computational cost. Probabilistic frameworks, such as Neural Processes (Garnelo et al., 2018) and Spatio-Temporal Point Processes (Chen et al., 2021), model data as unordered sets or discrete event intensities. Consequently, they either lack the explicit causal structure of recurrent systems or do not track the continuous evolution of signal values. In contrast to introducing expensive stochastic latent dynamics, we use Gaussian Processes solely as a robust smoothing mechanism to construct regularized control paths.

Efficient Integration and Structured Approaches. Algebraic approaches aim to optimize integration by summarizing input data over intervals. Neural Rough Differential Equations (Morrill et al., 2021) and Log-Neural CDEs (Walker et al., 2024) utilize signatures (Lyons, 1998) to effectively decouple the step size from the raw sampling rate. Other works focus on solver mechanics, such as relaxing error tolerances via seminorms (Kidger et al., 2021a), or architectural efficiency: Structured Linear CDEs (Walker et al., 2025) employ block-diagonal state transitions to accel-

erate vector field evaluations. We note that our Multi-View architecture shares this block-diagonal structure, but uses it to integrate multiple trajectory views simultaneously rather than for parallel associative scans. Finally, Neural Flows (Bilos et al., 2021) bypass iterative integration entirely by modeling the solution map directly. However, this eliminates the explicit causal structure necessary for adapting to evolving input streams. Unlike these methods, which focus on algebraic compression or bypassing the solver, our work targets the geometric irregularity of the input path itself as the primary source of numerical stiffness.

Latent Path Learning and Attention Mechanisms. While discrete transformers (Zhou et al., 2021; Wu et al., 2021) address long-term dependencies on fixed grids, continuous attention mechanisms—such as ContiFormer (Chen et al., 2023), Attentive NCDEs (Jhin et al., 2024), and MANODE (Havvaei et al., 2025) adapt this to irregular data. However, these methods primarily use attention to capture historical correlations or fuse multi-scale dynamics, often increasing computational cost. Similarly, generative frameworks like EXIT-NCDE (Jhin et al., 2022), Neural Lad (Li et al., 2023b), and stability-focused like DeNOTS (Kuleshov et al., 2024) prioritize expressivity or extrapolation, frequently at the expense of higher NFEs. In contrast, we employ attention not for temporal dependency modeling, but as a reconstruction mechanism. Inspired by Q-Former (Li et al., 2023a), our Multi-View architecture uses learnable queries to recover high-frequency information from explicitly smoothed control paths. While Log-Neural CDEs (Walker et al., 2024) address efficiency via algebraic summarization, our work establishes a parallel geometric alternative, demonstrating that path smoothing combined with attentive recovery offers a robust solution to the solver bottleneck.

Summary and Baselines. To rigorously evaluate our contribution, we select next baselines: GRU-D (Che et al., 2016), ODE-RNN (Rubanova et al., 2019), Linear and Cubic Neural CDEs (Kidger et al., 2020). Additionally, we include Log-NCDE (Walker et al., 2024) as a primary benchmark for computational efficiency. The critical research gap we address is the high sensitivity of adaptive solvers to input noise, which remains a bottleneck for standard Neural CDEs and is only indirectly addressed by algebraic signature-based methods. Our novelty lies in a decoupling integration cost from signal noise via smoothing, while recovering lost details through a multi-view attentive mechanism.

3. Method

3.1. Problem Formulation

We consider the task of supervised learning on time series. Let $\mathcal{S} = \{(t_k, \mathbf{x}_k)\}_{k=1}^N$ be an input sequence, where $t_k \in \mathbb{R}$

represent strictly increasing time stamps and $\mathbf{x}_k \in \mathbb{R}^d$ are observed feature vectors. The sampling rate is characterized by the time intervals $\Delta t_k = t_{k+1} - t_k$. It reduces to a constant Δt for regular series. The objective is to learn a mapping from \mathcal{S} to a target y . For simplicity, we assume that $t_1 = 0$ and $t_N = T$. The sequence is processed to obtain a latent embedding vector, which is subsequently passed to a linear classification or regression model to produce a prediction \hat{y} .

3.2. Neural Controlled Differential Equations

Neural CDE (Kidger et al., 2020) models the latent state $\mathbf{z}(t)$ as the solution to a differential equation driven by a continuous control path $\mathbf{X}(t) : [0, T] \rightarrow \mathbb{R}^d$, which is constructed by interpolating the discrete observations \mathcal{S} . The dynamics are governed by:

$$\mathbf{z}(T) = \mathbf{z}(0) + \int_0^T f_\theta(\mathbf{z}(t)) \frac{d\mathbf{X}(t)}{dt} dt, \quad (2)$$

where f_θ is a neural network parameterizing the vector field. The initial state $\mathbf{z}(0)$ is typically a learned linear projection of $\mathbf{X}(0)$. In practice, this integral is computed by an adaptive ODE solver (such as Dormand-Prince (Dormand & Prince, 1980; Hairer et al., 1993)) applied to the equivalent ODE system (1). These solvers dynamically adapt the step size $\eta_i = t_{i+1} - t_i$ to keep the Local Truncation Error (LTE) below a tolerance δ . To analyze the complexity, we first establish the relationship between control path regularity and solver step size.

Theorem 3.1 (NFE dependence on Control Path (informal)). *For an adaptive ODE solver (Dormand-Prince) of order p with error tolerance δ , the total NFE is proportional to the integral of the inverse step size:*

$$NFE \propto \int_0^T \left(\frac{1}{\delta} \left\| \frac{d^{p+1} \mathbf{X}(t)}{dt^{p+1}} \right\| \right)^{\frac{1}{p+1}} dt.$$

This theorem establishes that NFE is strictly determined by the $L_{1/(p+1)}$ -quasi-norm of the $(p+1)$ -th derivative of the control path.

3.3. Limitations of Deterministic Splines

Standard implementations construct $\mathbf{X}(t)$ using natural cubic splines or linear interpolation. While these methods guarantee $\mathbf{X}(t_k) = \mathbf{x}_k$, exact interpolation rigidly couples path regularity with input variations. Applying Theorem 3.1, we derive explicit complexity estimates over the fixed size interval $[0, T]$.

For linear and cubic splines, the integration cost scales with the first and second finite differences, respectively:

$$NFE_{lin} \propto \sum_k \|\Delta \mathbf{x}_k\|, \quad NFE_{cub} \propto \frac{1}{\Delta t} \sum_k \|\Delta^2 \mathbf{x}_k\|,$$

where $\Delta \mathbf{x}_k$ denotes the discrete derivative. In both cases, path roughness is determined by the input sequence. The solver is forced to traverse the exact geometry of the raw noisy observations, leading to a high NFE. See Figure 1 for a visualization of solver step distribution in standard splines.

3.4. Single Path Smoothing

To address the stiffness inherent to spline interpolation, we propose methods that decouple the trajectory smoothness from the input data. We first introduce Kernel Smoothing as a baseline to motivate the decoupling, then present Gaussian Process Smoothing, which constitutes our contribution.

Kernel Smoothing. We employ the Nadaraya-Watson estimator with a Gaussian Radial Basis Function (RBF) kernel $k_h(t, t') = \exp\left(-\frac{(t-t')^2}{2h^2}\right)$ to construct a smooth path $X_{\text{kernel}}(t)$. Given a bandwidth parameter h , the path is defined as:

$$\mathbf{X}_{\text{kernel}}(t) = \frac{\sum_{k=1}^N k_h(t - t_k) \mathbf{x}_k}{\sum_{j=1}^N k_h(t - t_j)}.$$

Gaussian Process (GP) Smoothing. Alternatively, we place a GP prior on the underlying signal, $\mathbf{X}_{GP}(t) \sim \mathcal{GP}(0, k(t, t'))$. We utilize the same kernel defined above. The control path $\mathbf{X}_{GP}(t)$ is the posterior mean function conditioned on the observations \mathcal{S} with assumed Gaussian noise variance σ^2 . It is computed as:

$$\mathbf{X}_{GP}(t) = \mathbf{k}_h(t)^\top (\mathbf{K}_h + \sigma^2 \mathbf{I})^{-1} \mathbf{X},$$

where $\mathbf{X} \in \mathbb{R}^{N \times d}$ is the matrix of stacked feature vectors. The kernel vector $\mathbf{k}_h(t)$ and Gram matrix \mathbf{K}_h are defined as in standard GP regression.

While exact GP inference has cubic complexity $\mathcal{O}(N^3)$ with respect to sequence length due to matrix inversion, this is a static, one-time preprocessing cost. This initialization overhead remains negligible compared to the integration efficiency gains. As proven in Appendix A.5, GPs provide

the optimal linear reconstruction, justifying the cubic preprocessing cost by ensuring that the smoothed trajectory remains maximally faithful to the underlying signal compared to heuristic kernel estimates.

Theorem 3.2 (Derivative Bounds for Smoothing Kernels). *Let $\mathbf{X}_h(t)$ be constructed via Nadaraya-Watson regression or as the posterior mean of a GP with a stationary RBF kernel with lengthscale h . The p -th derivative of the trajectory satisfies the uniform bound:*

$$\sup_{t \in [0, T]} \left\| \frac{d^p \mathbf{X}_h(t)}{dt^p} \right\| \leq \frac{C_p}{h^p} \|\mathbf{X}\|_\infty,$$

where C_p is a constant depending on the kernel shape and $\|\mathbf{X}\|_\infty$ is the bound on observations.

Corollary 3.3 (Smoothing NFE Scaling). *Substituting the bound from Theorem 3.2 into the NFE integral (Theorem 3.1) with $k = p + 1$ yields:*

$$\text{NFE}(\mathbf{X}_h(t)) \propto \int_0^T \left(h^{-(p+1)} \right)^{\frac{1}{p+1}} dt \propto h^{-1}.$$

The selection of the h is critical. In our proposed Multi-View architecture (Section 3.5), we do not rely on a single h , but rather employ a spectrum of parameters to capture multi-scale dynamics.

3.5. Multi-View Architecture

Overview and Motivation. Standard smoothing can eliminate high-frequency information that may be relevant to the prediction task. To mitigate information loss, we propose a Multi-View CDE (MV-CDE) architecture that integrates multiple distinct trajectories simultaneously. See the complete pipeline is illustrated in Figure 2. Furthermore, to incorporate local temporal context, we introduce the Multi-View Convolutional CDE (MVC-CDE) extension. Rather than relying on a single smoothed approximation, these frameworks construct a set of paths differentiated by their attention weights and smoothness parameters.

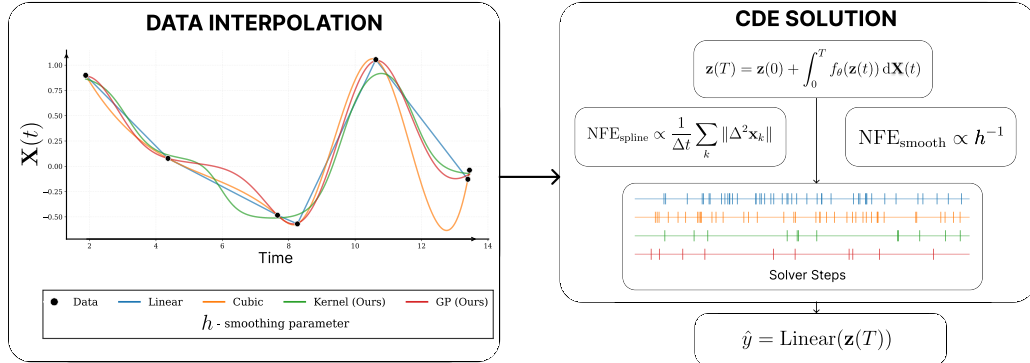


Figure 1. Standard Neural CDE pipeline for different types of path construction.

Feature Extraction and Convolution. Applying interpolation weights based solely on raw pointwise values may fail to capture complex local temporal dependencies. To address this, we introduce an optional feature-extraction stage. Let \mathbf{u}_k denote a context vector associated with the observation \mathbf{x}_k .

In the basic MV-CDE setting, the model computes attention scores directly from raw observations, setting $\mathbf{u}_k = \mathbf{x}_k$. For MVC-CDE, we better account for temporal neighborhood information by employing a 1D convolutional learnable neural network Φ_{conv} with a fixed kernel size. Following the VGG design principles (Simonyan & Zisserman, 2015), we use small kernels to efficiently capture local context. This network performs discrete temporal convolutions over the input sequence \mathcal{S} to produce a sequence of latent descriptors:

$$\{\mathbf{u}_k\}_{k=1}^N = \Phi_{\text{conv}}(\{\mathbf{x}_k\}_{k=1}^N).$$

Specifically, these descriptors \mathbf{u}_k are used exclusively to determine the attention weights of each observation. The continuous control path $\mathbf{X}^{(m)}(t)$ itself remains a function of the original observations \mathbf{x}_k , preserving the interpretability and dimensionality of the input signal.

Weighted Paths. To capture multi-scale dynamics without over-smoothing, we introduce a multi-head architecture. Inspired by the Querying Transformer (Q-Former) from vision-language modeling (Li et al., 2023a), we employ a set of learnable queries to extract relevant temporal features. We define M learnable query vectors $\mathbf{Q} = [\mathbf{q}_1, \dots, \mathbf{q}_M] \in \mathbb{R}^{M \times d_{\text{ctx}}}$, where d_{ctx} is the dimension of \mathbf{u}_k . For each head m , we compute attention scores $\alpha_{m,k}$ using the context vectors \mathbf{u}_k :

$$\alpha_{m,k} = \text{softmax}_k \left(\frac{\mathbf{q}_m^\top \mathbf{u}_k}{\sqrt{d_{\text{ctx}}}} \right).$$

These attention weights determine the relevance of each observation for the m -th trajectory. We construct M distinct continuous paths $\mathbf{X}^{(m)}(t)$, utilizing the chosen smoothing scheme. Therefore, we state Weighted Interpolation schemes applied to the original observations \mathbf{x}_k :

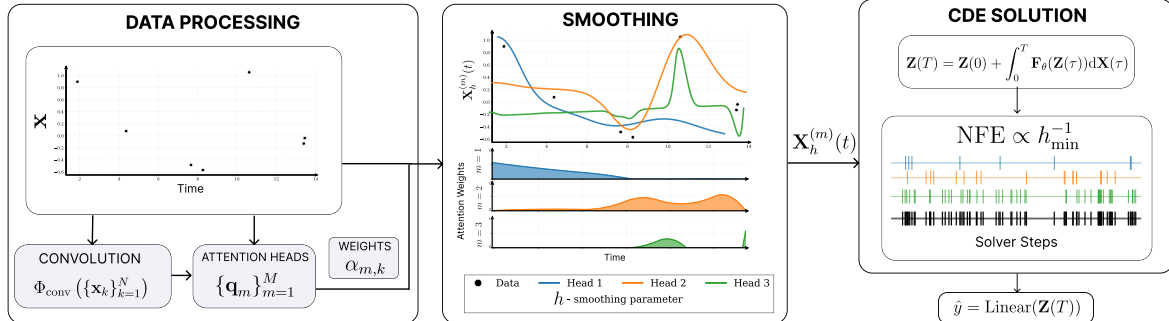


Figure 2. Proposed MV-CDE and MVC-CDE architectures.

Weighted Kernel Path. The weights modify the kernel density estimate (Cai, 2001):

$$\mathbf{X}^{(m)}(t) = \frac{\sum_{k=1}^N \alpha_{m,k} k_{h_m}(t - t_k) \mathbf{x}_k}{\sum_{j=1}^N \alpha_{m,j} k_{h_m}(t - t_j)}. \quad (3)$$

Weighted GP Path. We introduce heteroscedastic noise into the GP posterior formulation (Lázaro-Gredilla & Titsias, 2011; Le et al., 2005). We define a diagonal noise covariance matrix Σ_m where the noise variance for the k -th observation is inversely proportional to its attention score:

$$(\Sigma_m)_{kk} = \frac{\sigma_{\text{base}}^2}{\alpha_{m,k} + \epsilon}.$$

Observations with high attention scores are treated as high-precision points with low noise variance, while low-attention points are filtered out as noise.

$$\mathbf{X}^{(m)}(t) = \mathbf{k}_h(t)^\top (\mathbf{K}_h + \Sigma_m)^{-1} \mathbf{X}, \quad (4)$$

where the kernel structures \mathbf{k}_{h_m} and \mathbf{K}_{h_m} follow the definitions in Section 3.4, parameterized by head-specific lengthscales h_m , while \mathbf{X} remains the shared observation matrix.

Parallel Integration. The proposed architecture generates a set of M control paths $\{\mathbf{X}^{(m)}(t)\}_{m=1}^M$. These paths are integrated simultaneously within a single ODE solver call. We define the global latent state $\mathbf{Z}(t)$ as the concatenation of the individual head states:

$$\mathbf{Z}(t) = [\mathbf{z}^{(1)}(t), \dots, \mathbf{z}^{(M)}(t)] \in \mathbb{R}^{M \cdot d_{\text{hidden}}}.$$

Each head evolves according to its own parameterised vector field f_{θ_m} . The combined differential equation is:

$$\frac{d\mathbf{Z}(t)}{dt} = \text{Concat}_{m=1}^M \left(f_{\theta_m}(\mathbf{z}^{(m)}(t)) \frac{d\mathbf{X}^{(m)}(t)}{dt} \right). \quad (5)$$

This approach essentially treats the system as a block-diagonal ODE (Walker et al., 2025), where independent dynamics are solved jointly. It leads to the next theorem:

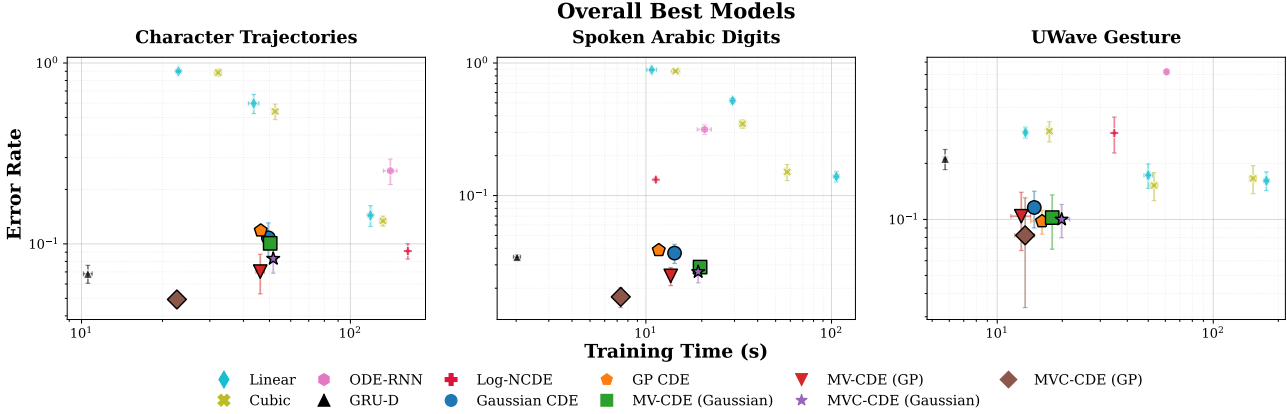


Figure 3. Pareto Efficiency Plot. Error Rate (log scale) versus Total Training Time (log scale).

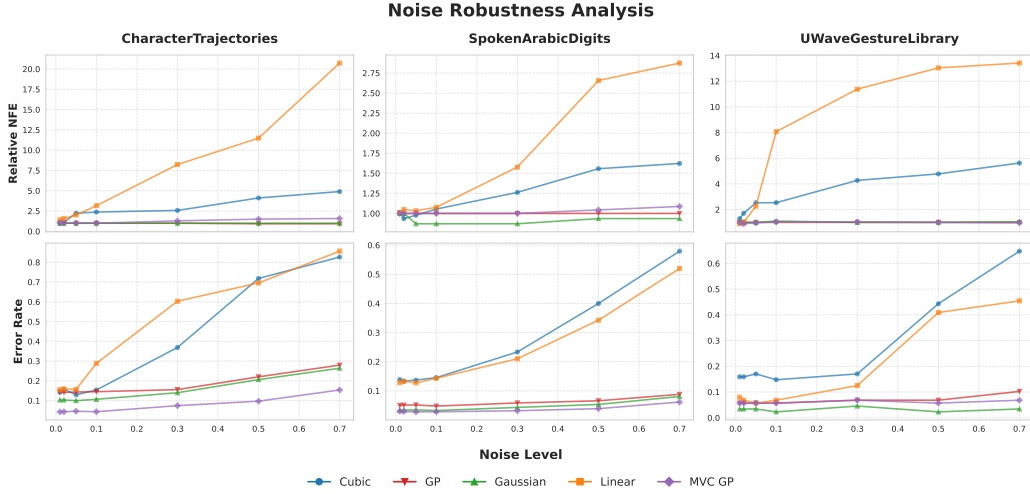


Figure 4. Noise Robustness Analysis. The plots compare the stability of different path-construction methods under varying intensities of additive white Gaussian noise. Top row: Relative NFE normalized to the noise-free number. Bottom row: Classification error rate.

Theorem 3.4 (Parallel Integration Bottleneck). *Consider an adaptive ODE solver integrating the block-diagonal system (5) with $\mathbf{Z}(t)$ with a global error tolerance δ . The total NFE is strictly governed by the minimum smoothing parameter in the ensemble:*

$$NFE_{total} \propto \left(\min_{m=[1;M]} h_m \right)^{-1}.$$

This formulation highlights a critical design choice. While including heads with very small h_m allows for capturing fine-grained details, it increases the overall computational cost. By optimizing h_m , our method balances multi-view representation capability with integration speed. To justify the use of $M > 1$, we observe that single-head models often fail to capture diverse temporal features, while multiple heads provide robustness through ensemble representations.

Pipeline Summary. The forward pass begins with an en-

coding step that maps the input \mathbf{x}_k to \mathbf{u}_k via a CNN or an identity function. This is followed by an attention mechanism that computes M -head scores $\alpha_{m,k}$ using learnable queries. These scores are subsequently used in a smoothing phase to generate continuous paths $\mathbf{X}^{(m)}(t)$ through weighted Gaussian processes (4) or kernel regression (3). Finally, the integration step yields the prediction by solving a block-diagonal NCDE driven by the concatenation of these smooth paths.

4. Results

In this section, we present the comparative performance of our proposed architectures against the baselines. We primarily focus on classification accuracy and computational efficiency, followed by an ablation study and an analysis of model interpretability.

For detailed experimental settings and dataset descriptions,

we refer to Appendix B.

4.1. Main Performance Comparison

We evaluated our method across three diverse benchmarks from the UEA Time Series Archive (Bagnall et al., 2018), selected to cover a broad spectrum of signal characteristics. Low-dimensional **CharacterTrajectories** captures high-frequency pen-tip dynamics; High-dimensional **SpokenArabicDigits** represents speech feature coefficients; and longer-range **UWaveGestureLibrary** involves complex human movement patterns. This selection enables us to rigorously assess the robustness of our path-smoothing and attention mechanisms across varying regimes of trajectory roughness, feature dimensionality, and temporal resolution. See Table 1 for detailed numerical results. The proposed **MVC-CDE (GP)** consistently achieves SOTA accuracy and significantly outperforms the baselines. The best models comparison in Figure 3 also supports the evidence that our method attains the best accuracies and efficiency.

4.2. Computational Efficiency

Our method results in substantial training speedups compared to baselines. As shown in our experiments in Figure 3, MVC-GP demonstrates a speedup ranging from $4.3\times$ to $14.5\times$ compared to standard CDE methods, and up to $16\times$ faster than ODE-RNN on complex tasks like *UWaveGestureLibrary*, while requiring significantly fewer NFE to solve the underlying differential equations. To ensure a fair comparison, we include multiple points for Linear and Cubic baselines by varying their solver tolerances; this demonstrates that their efficiency cannot be matched by simply reducing numerical precision without a significant loss in accuracy.

These results confirm that MVC-GP not only improves classification performance but also ensures high computational efficiency, making it suitable for scalable time-series modeling.

4.3. Noise Robustness Analysis

To evaluate the stability of path-construction mechanisms under perturbation, we subject the best-performing models to a robustness test. We inject additive white Gaussian noise into the test set features, sweeping the noise level across a range of intensities. We monitor both the degradation in test accuracy and the variation in the Average NFE in Figure 4.

The results confirm the hypothesis that smoothing-based methods maintain efficient solver dynamics. As illustrated in Figure 4, direct interpolation methods exhibit a drastic increase in NFE and error rates as noise increases. In contrast, our smoothing approach ensures that the NFE remains almost constant and the error rate degradation is significantly slower, demonstrating superior robustness to noisy inputs.

4.4. Impact of Head Number and Smoothing

To understand the scalability of the Multi-View architecture, we analyzed how model performance depends on the number of attention heads and the smoothing bandwidth h . In this experiment, all heads are initialized with the same bandwidth h , and we observe the effect of increasing M from 1 to 8.

As illustrated in Figure 6, increasing the number of heads generally reduces error rates across all datasets. This effect is most pronounced in configurations with high smoothing parameters, where a single head’s focus results in significant information loss due to over-smoothing. By increasing M , the attention mechanism enables the solver to leverage multiple representations of the smoothed trajectory, effectively recovering performance.

However, the performance gain follows a law of diminishing returns. We observe that for configurations with GP interpolation, the error rate tends to plateau around $M = 4$.

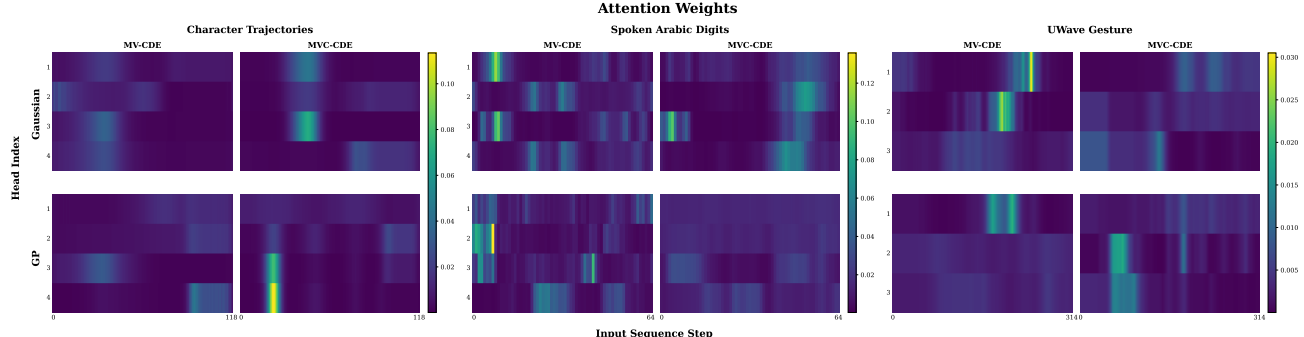


Figure 5. Learned Attention Weights across Datasets. The heatmaps visualize the example of learned attention weights for one sample example assigned to different smoothing heads over time.

4.5. Interpretability and Attention Dynamics

Figure 5 compares the attention patterns of the trained MV model against the MVC architecture.

Dataset-Specific Dynamics. The behavior of the attention heads varies distinctly across datasets, reflecting the nature of the underlying signals:

- **CharacterTrajectories (Low-Dimensional):** The contrast is most visible here: MV attention is blurry, whereas MVC exhibits sharp, localized activations, effectively filtering the trajectory into distinct temporal events.
- **SpokenArabicDigits (High-Dimensional):** As shown in Figure 5, the MV maps are dominated by high-frequency vertical striations induced by the high dimensionality of the input. This pattern indicates that the model reacts to noise and raw signal jumps at individual timestamps. In contrast, MVC smoothes out local noise via convolutions, allowing the attention mechanism to focus on more robust, longer-term features.
- **UWaveGestureLibrary (Long Sequences):** Both models capture the periodic nature of the gesture data characteristic of long sequences. While the sheer length of the signal makes specific head interpretation less distinct than in shorter tasks, MVC specifically benefits from the input’s low dimensionality. This allows it to effectively leverage multi-head capabilities to isolate different aspects of the signal despite the temporal complexity.

4.6. Other ablation studies

Supplementary ablation studies, including single-kernel baselines and granular computational cost analysis, are provided in Appendix C.

5. Conclusion

In this work, we addressed the fundamental trade-off between trajectory regularity and representation power in Neural CDEs. We identified that standard interpolation schemes induce numerical stiffness, forcing adaptive solvers to perform excessive function evaluations. To overcome this, we proposed MVC-CDE, a novel architecture that replaces deterministic splines with attentive multi-scale smoothing. By dynamically aggregating information from multiple regularized GP paths, our method effectively decouples the integration cost from input noise. Empirical evaluations on real-world benchmarks demonstrate that MVC-CDE achieves SOTA accuracy while reducing the Number of Function Evaluations by up to an order of magnitude. These results establish path smoothing not merely as a preprocessing heuristic but as a critical architectural component for scalable, efficient continuous-time sequence modeling.

Impact Statement

This paper presents work whose goal is to advance the field of Machine Learning. There are many potential societal consequences of our work, none which we feel must be specifically highlighted here.

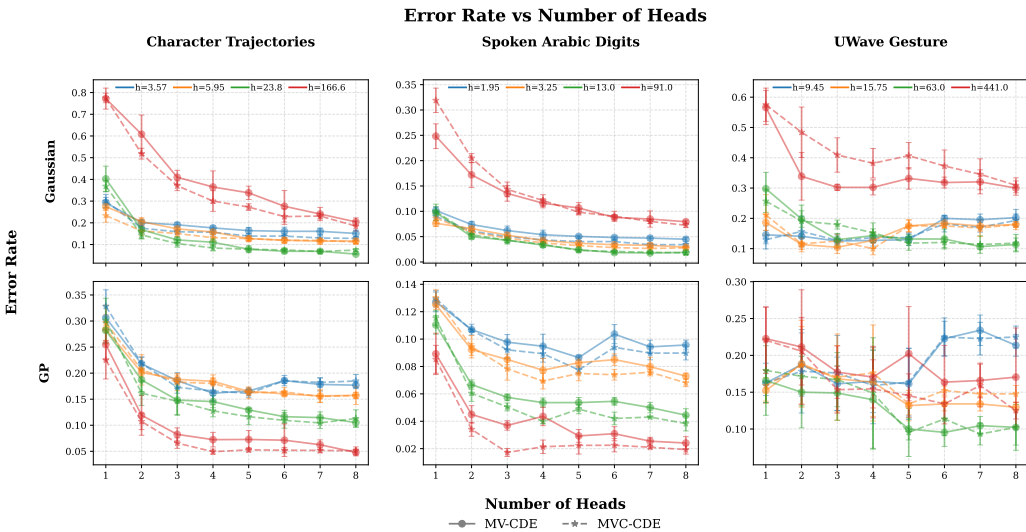


Figure 6. Ablation: Impact of Head Count. The plots display the error rate as a function of the number of heads across different fixed smoothing bandwidths h for MV-CDE and MVC-CDE.

References

Bagnall, A. J., Dau, H. A., Lines, J., Flynn, M., Large, J., Bostrom, A., Southam, P., and Keogh, E. J. The UEA multivariate time series classification archive, 2018. *CoRR*, abs/1811.00075, 2018. URL <http://arxiv.org/abs/1811.00075>.

Bilos, M., Sommer, J., Rangapuram, S. S., Januschowski, T., and Günnemann, S. Neural flows: Efficient alternative to neural odes. In Ranzato, M., Beygelzimer, A., Dauphin, Y. N., Liang, P., and Vaughan, J. W. (eds.), *Advances in Neural Information Processing Systems 34: Annual Conference on Neural Information Processing Systems 2021, NeurIPS 2021, December 6-14, 2021, virtual*, pp. 21325–21337, 2021. URL <https://proceedings.neurips.cc/paper/2021/hash/b21f9f98829dea9a48fd8aaddc1f159d-Abstract.html>.

Cai, Z. Weighted nadaraya–watson regression estimation. *Statistics & Probability Letters*, 51:307–318, 2001. URL <https://api.semanticscholar.org/CorpusID:12425264>.

Che, Z., Purushotham, S., Cho, K., Sontag, D. A., and Liu, Y. Recurrent neural networks for multivariate time series with missing values. *Scientific Reports*, 8, 2016. URL <https://api.semanticscholar.org/CorpusID:4900015>.

Chen, R. T. Q., Amos, B., and Nickel, M. Neural spatio-temporal point processes. In *9th International Conference on Learning Representations, ICLR 2021, Virtual Event, Austria, May 3-7, 2021*. OpenReview.net, 2021. URL <https://openreview.net/forum?id=XQQA6-So14>.

Chen, T. Q., Rubanova, Y., Bettencourt, J., and Duvenaud, D. Neural ordinary differential equations. In Bengio, S., Wallach, H. M., Larochelle, H., Grauman, K., Cesa-Bianchi, N., and Garnett, R. (eds.), *Advances in Neural Information Processing Systems 31: Annual Conference on Neural Information Processing Systems 2018, NeurIPS 2018, December 3-8, 2018, Montréal, Canada*, pp. 6572–6583, 2018. URL <https://proceedings.neurips.cc/paper/2018/hash/69386f6bb1dfed68692a24c8686939b9-Abstract.html>.

Chen, Y., Ren, K., Wang, Y., Fang, Y., Sun, W., and Li, D. Contiformer: Continuous-time transformer for irregular time series modeling. 2023. URL https://papers.nips.cc/paper_files/paper/2023/hash/9328208f88ec69420031647e6ff97727-Abstract.html.

Dau, H. A., Bagnall, A. J., Kamgar, K., Yeh, C. M., Zhu, Y., Gharghabi, S., Ratanamahatana, C. A., and Keogh, E. J. The UCR time series archive. *IEEE CAA J. Autom. Sinica*, 6(6):1293–1305, 2019. doi: 10.1109/JAS.2019.1911747. URL <https://doi.org/10.1109/jas.2019.1911747>.

de Boor, C. *A Practical Guide to Splines*. Applied Mathematical Sciences. Springer, 1978. ISBN 978-1-4612-6333-3. doi: 10.1007/978-1-4612-6333-3. URL <https://doi.org/10.1007/978-1-4612-6333-3>.

Dormand, J. R. and Prince, P. J. A family of embedded runge-kutta formulae. *Journal of Computational and Applied Mathematics*, 6:19–26, 1980. URL <https://api.semanticscholar.org/CorpusID:122754533>.

Finlay, C., Jacobsen, J., Nurbekyan, L., and Oberman, A. M. How to train your neural ODE: the world of jacobian and kinetic regularization. In *Proceedings of the 37th International Conference on Machine Learning, ICML 2020, 13-18 July 2020, Virtual Event*, volume 119 of *Proceedings of Machine Learning Research*, pp. 3154–3164. PMLR, 2020. URL <http://proceedings.mlr.press/v119/finlay20a.html>.

Garnelo, M., Schwarz, J., Rosenbaum, D., Viola, F., Rezende, D. J., Eslami, S. M. A., and Teh, Y. W. Neural processes. *CoRR*, abs/1807.01622, 2018. URL <http://arxiv.org/abs/1807.01622>.

Ghosh, A., Behl, H. S., Dupont, E., Torr, P. H. S., and Namboodiri, V. P. STEER : Simple temporal regularization for neural odes. *CoRR*, abs/2006.10711, 2020. URL <https://arxiv.org/abs/2006.10711>.

Hairer, E., Nørsett, S. P., and Wanner, G. Solving ordinary differential equations i (2nd revised ed.): nonstiff problems. 1993. URL <https://api.semanticscholar.org/CorpusID:116791328>.

Harutyunyan, H., Khachatrian, H., Kale, D. C., and Galstyan, A. Multitask learning and benchmarking with clinical time series data. *CoRR*, abs/1703.07771, 2017. URL <http://arxiv.org/abs/1703.07771>.

Havaei, M. A., Shahhosseini, V., and Maknoon, R. Continuous-time air pollutant forecasting using multi-timescale attention neural ordinary differential equations (ma-node). *Scientific Reports*, 15, 2025. URL <https://api.semanticscholar.org/CorpusID:284046397>.

Jin, S., Lee, J., Jo, M., Kook, S., Jeon, J., Hyeong, J., Kim, J., and Park, N. EXIT: extrapolation and

interpolation-based neural controlled differential equations for time-series classification and forecasting. In Laforest, F., Troncy, R., Simperl, E., Agarwal, D., Gionis, A., Herman, I., and Médini, L. (eds.), *WWW '22: The ACM Web Conference 2022, Virtual Event, Lyon, France, April 25 - 29, 2022*, pp. 3102–3112. ACM, 2022. doi: 10.1145/3485447.3512030. URL <https://doi.org/10.1145/3485447.3512030>.

Jhin, S. Y., Shin, H., Kim, S., Hong, S., Jo, M., Park, S., Park, N., Lee, S., Maeng, H., and Jeon, S. Attentive neural controlled differential equations for time-series classification and forecasting. *Knowl. Inf. Syst.*, 66(3):1885–1915, 2024. doi: 10.1007/S10115-023-01977-5. URL <https://doi.org/10.1007/s10115-023-01977-5>.

Kelly, J., Bettencourt, J., Johnson, M. J., and Duvenaud, D. Learning differential equations that are easy to solve. 2020. URL <https://proceedings.neurips.cc/paper/2020/hash/2e255d2d6bf9bb33030246d31f1a79ca-Abstract.html>.

Kidger, P., Morrill, J., Foster, J., and Lyons, T. J. Neural controlled differential equations for irregular time series. In Larochelle, H., Ranzato, M., Hadsell, R., Balcan, M., and Lin, H. (eds.), *Advances in Neural Information Processing Systems 33: Annual Conference on Neural Information Processing Systems 2020, NeurIPS 2020, December 6-12, 2020, virtual*, 2020. URL <https://proceedings.neurips.cc/paper/2020/hash/4a5876b450b45371f6cfe5047ac8cd45-Abstract.html>.

Kidger, P., Chen, R. T. Q., and Lyons, T. J. "hey, that's not an ode": Faster ODE adjoints via seminorms. In Meila, M. and Zhang, T. (eds.), *Proceedings of the 38th International Conference on Machine Learning, ICML 2021, 18-24 July 2021, Virtual Event*, volume 139 of *Proceedings of Machine Learning Research*, pp. 5443–5452. PMLR, 2021a. URL <http://proceedings.mlr.press/v139/kidger21a.html>.

Kidger, P., Foster, J., Li, X., and Lyons, T. J. Efficient and accurate gradients for neural sdes. In Ranzato, M., Beygelzimer, A., Dauphin, Y. N., Liang, P., and Vaughan, J. W. (eds.), *Advances in Neural Information Processing Systems 34: Annual Conference on Neural Information Processing Systems 2021, NeurIPS 2021, December 6-14, 2021, virtual*, pp. 18747–18761, 2021b. URL <https://proceedings.neurips.cc/paper/2021/hash/9ba196c7a6e89eaf0d0954de80fc1b224-Abstract.html>.

Kloeden, P. E. and Pearson, R. A. The numerical solution of stochastic differential equations. *The Journal of the Australian Mathematical Society. Series B. Applied Mathematics*, 20(1):8–12, 1977. doi: 10.1017/S0334270000001405.

Kuleshov, I., Romanenkova, E., Zhuzhel, V., Boeva, G., Vorsin, E., and Zaytsev, A. Denots: Stable deep neural odes for time series. *arXiv preprint arXiv:2408.08055*, 2024.

Lázaro-Gredilla, M. and Titsias, M. K. Variational heteroscedastic gaussian process regression. In Getoor, L. and Scheffer, T. (eds.), *Proceedings of the 28th International Conference on Machine Learning, ICML 2011, Bellevue, Washington, USA, June 28 - July 2, 2011*, pp. 841–848. Omnipress, 2011. URL https://icml.cc/2011/papers/456_icmlpaper.pdf.

Le, Q. V., Smola, A. J., and Canu, S. Heteroscedastic gaussian process regression. In Raedt, L. D. and Wrobel, S. (eds.), *Machine Learning, Proceedings of the Twenty-Second International Conference (ICML 2005), Bonn, Germany, August 7-11, 2005*, volume 119 of *ACM International Conference Proceeding Series*, pp. 489–496. ACM, 2005. doi: 10.1145/1102351.1102413. URL <https://doi.org/10.1145/1102351.1102413>.

Li, J., Li, D., Savarese, S., and Hoi, S. C. H. BLIP-2: bootstrapping language-image pre-training with frozen image encoders and large language models. In Krause, A., Brunskill, E., Cho, K., Engelhardt, B., Sabato, S., and Scarlett, J. (eds.), *International Conference on Machine Learning, ICML 2023, 23-29 July 2023, Honolulu, Hawaii, USA*, volume 202 of *Proceedings of Machine Learning Research*, pp. 19730–19742. PMLR, 2023a. URL <https://proceedings.mlr.press/v202/li23q.html>.

Li, T., Li, J., and Zhu, Z. Neural lad: A neural latent dynamics framework for times series modeling. In Oh, A., Naumann, T., Globerson, A., Saenko, K., Hardt, M., and Levine, S. (eds.), *Advances in Neural Information Processing Systems 36: Annual Conference on Neural Information Processing Systems 2023, NeurIPS 2023, New Orleans, LA, USA, December 10 - 16, 2023*, 2023b. URL http://papers.nips.cc/paper_files/paper/2023/hash/382a8606a85ca6ec7c06185a1a95ce8b-Abstract-Conference.html.

Li, X., Wong, T. L., Chen, R. T. Q., and Duvenaud, D. Scalable gradients for stochastic differential equations. In Chiappa, S. and Calandri, R. (eds.), *The 23rd International Conference on Artificial Intelligence and Statistics, AIS-TATS 2020, 26-28 August 2020, Online [Palermo, Sicily*,

Italy], volume 108 of *Proceedings of Machine Learning Research*, pp. 3870–3882. PMLR, 2020. URL <http://proceedings.mlr.press/v108/li20i.html>.

Lyons, T. J. Differential equations driven by rough signals. *Revista Matemática Iberoamericana*, 14(2):215–310, 1998. URL <http://eudml.org/doc/39555>.

Morrill, J., Salvi, C., Kidger, P., and Foster, J. Neural rough differential equations for long time series. In Meila, M. and Zhang, T. (eds.), *Proceedings of the 38th International Conference on Machine Learning, ICML 2021, 18-24 July 2021, Virtual Event*, volume 139 of *Proceedings of Machine Learning Research*, pp. 7829–7838. PMLR, 2021. URL <http://proceedings.mlr.press/v139/morrill21b.html>.

Morrill, J., Kidger, P., Yang, L., and Lyons, T. J. On the choice of interpolation scheme for neural cdes. *Trans. Mach. Learn. Res.*, 2022, 2022. URL <https://openreview.net/forum?id=caRBFhxXIG>.

Oh, Y., Kam, S., Lee, J., Lim, D., Kim, S., and Bui, A. A. T. Comprehensive review of neural differential equations for time series analysis. In *Proceedings of the Thirty-Fourth International Joint Conference on Artificial Intelligence, IJCAI 2025, Montreal, Canada, August 16-22, 2025*, pp. 10621–10631. ijcai.org, 2025. doi: 10.24963/IJCAI.2025/1179. URL <https://doi.org/10.24963/ijcai.2025/1179>.

Raissi, M., Perdikaris, P., and Karniadakis, G. E. Physics-informed neural networks: A deep learning framework for solving forward and inverse problems involving nonlinear partial differential equations. *J. Comput. Phys.*, 378:686–707, 2019. URL <https://api.semanticscholar.org/CorpusID:57379996>.

Rasmussen, C. E. and Williams, C. K. I. *Gaussian processes for machine learning*. Adaptive computation and machine learning. MIT Press, 2006. ISBN 026218253X. URL <https://www.worldcat.org/oclc/61285753>.

Reinsch, C. H. Smoothing by spline functions. *Numerische Mathematik*, 10:177–183, 1967. URL <https://api.semanticscholar.org/CorpusID:26555189>.

Rubanova, Y., Chen, T. Q., and Duvenaud, D. Latent ordinary differential equations for irregularly-sampled time series. In Wallach, H. M., Larochelle, H., Beygelzimer, A., d’Alché-Buc, F., Fox, E. B., and Garnett, R. (eds.), *Advances in Neural Information Processing Systems 32: Annual Conference on Neural Information Processing Systems 2019, NeurIPS 2019, December 8-14, 2019, Vancouver, BC, Canada*, pp. 5321–5331, 2019. URL <https://proceedings.neurips.cc/paper/2019/hash/42a6845a557bef704ad8ac9cb4461d43-Abstract.html>.

Simonyan, K. and Zisserman, A. Very deep convolutional networks for large-scale image recognition. 2015. URL <http://arxiv.org/abs/1409.1556>.

Tsybakov, A. Introduction to nonparametric estimation. In *Springer Series in Statistics*, 2008. URL <https://api.semanticscholar.org/CorpusID:42933599>.

Wahba, G. *Spline Models for Observational Data*. SIAM, 1990. ISBN 978-0-89871-244-5. doi: 10.1137/1.9781611970128. URL <https://doi.org/10.1137/1.9781611970128>.

Walker, B., McLeod, A. D., Qin, T., Cheng, Y., Li, H., and Lyons, T. J. Log neural controlled differential equations: The lie brackets make A difference. In *Forty-first International Conference on Machine Learning, ICML 2024, Vienna, Austria, July 21-27, 2024*. OpenReview.net, 2024. URL <https://openreview.net/forum?id=0tYrMtQyPT>.

Walker, B., Yang, L., Cirone, N. M., Salvi, C., and Lyons, T. J. Structured linear cdes: Maximally expressive and parallel-in-time sequence models. *CoRR*, abs/2505.17761, 2025. doi: 10.48550/ARXIV.2505.17761. URL <https://doi.org/10.48550/arXiv.2505.17761>.

Wand, M. P. and Jones, M. C. Kernel smoothing. 1995. URL <https://api.semanticscholar.org/CorpusID:198189892>.

Wu, H., Xu, J., Wang, J., and Long, M. Autoformer: Decomposition transformers with auto-correlation for long-term series forecasting. In Ranzato, M., Beygelzimer, A., Dauphin, Y. N., Liang, P., and Vaughan, J. W. (eds.), *Advances in Neural Information Processing Systems 34: Annual Conference on Neural Information Processing Systems 2021, NeurIPS 2021, December 6-14, 2021, virtual*, pp. 22419–22430, 2021. URL <https://proceedings.neurips.cc/paper/2021/hash/bcc0d400288793e8bcd7c19a8ac0c2b-Abstract.html>.

Zhang, Z., Zohren, S., and Roberts, S. J. Deeplob: Deep convolutional neural networks for limit order books. *IEEE Transactions on Signal Processing*, 67:3001–3012, 2018. URL <https://api.semanticscholar.org/CorpusID:85498429>.

Zhou, H., Zhang, S., Peng, J., Zhang, S., Li, J., Xiong, H., and Zhang, W. Informer: Beyond efficient transformer for long sequence time-series forecasting. In

Thirty-Fifth AAAI Conference on Artificial Intelligence, AAAI 2021, Thirty-Third Conference on Innovative Applications of Artificial Intelligence, IAAI 2021, The Eleventh Symposium on Educational Advances in Artificial Intelligence, EAAI 2021, Virtual Event, February 2-9, 2021, pp. 11106–11115. AAAI Press, 2021. doi: 10.1609/AAAI.V35I12.17325. URL <https://doi.org/10.1609/aaai.v35i12.17325>.

A. Theoretical Analysis of Path Regularity and Solver Complexity

In this section, we provide a rigorous analysis of the computational complexity of Neural CDEs. We bridge the gap between the analytic properties of the control path $\mathbf{X}(t)$, specifically its Sobolev regularity, and the discrete behavior of adaptive ODE solvers. We derive explicit complexity bounds for deterministic interpolants versus the proposed smoothing priors and formally prove the bottleneck effect in the MV-CDE architecture.

A.1. ODE Solver Dynamics and Step Size Control

The computational cost of a Neural CDE is dominated by the numerical integration of the latent state $\mathbf{z}(t)$ governed by Eq. (2). Modern implementations employ embedded Runge-Kutta methods, such as the Dormand-Prince pair (Dopri5) of order $p = 5$ (Dormand & Prince, 1980). These solvers dynamically adapt the step size $\eta_i = t_{i+1} - t_i$ to ensure the Local Truncation Error (LTE) remains below a specified tolerance δ .

Theorem (3.1). [Step Size dependence on Control Regularity] For a numerical method of order p , the asymptotic local truncation error at step i is governed by the principal error function involving the $(p+1)$ -th derivative of the solution (Hairer et al., 1993):

$$\text{LTE}_i = C \cdot \eta_i^{p+1} \left\| \frac{d^{p+1} \mathbf{z}(t)}{dt^{p+1}} \right\| + \mathcal{O}(\eta_i^{p+2}), \quad (6)$$

where C is a method-dependent constant. Since $\mathbf{z}(t)$ is driven by $\mathbf{X}(t)$, the chain rule implies that higher-order derivatives of the state scale linearly with the higher-order derivatives of the control path. Specifically, assuming the vector field f_θ is Lipschitz continuous and bounded, we have $\left\| \frac{d^{p+1} \mathbf{z}}{dt^{p+1}} \right\| \propto \left\| \frac{d^{p+1} \mathbf{X}}{dt^{p+1}} \right\|$. To satisfy the condition $\text{LTE}_i \leq \delta$, the adaptive step size η_i must satisfy:

$$\eta_i \leq \left(\frac{\delta}{C \cdot \left\| \mathbf{X}^{(p+1)}(t_i) \right\|} \right)^{\frac{1}{p+1}}. \quad (7)$$

The total NFE is proportional to the number of steps required to traverse $[0, T]$. In the continuous limit, this relates to the integral of the inverse step size:

$$\text{NFE} \propto \int_0^T \frac{1}{\eta(t)} dt \propto \int_0^T \left\| \frac{d^{p+1} \mathbf{X}(t)}{dt^{p+1}} \right\|^{-\frac{1}{p+1}} dt. \quad (8)$$

This establishes that NFE is strictly determined by the $L_{1/(p+1)}$ -quasi-norm of the $(p+1)$ -th derivative of the control path. Unbounded or large derivatives force $\eta \rightarrow 0$, causing NFE to diverge.

A.2. Regularity of Deterministic Interpolation

Standard Neural CDEs utilize linear or natural cubic splines (de Boor, 1978; Reinsch, 1967) to construct $\mathbf{X}(t)$ from discrete observations $\mathcal{S} = \{(t_k, \mathbf{x}_k)\}_{k=1}^N$. We analyze the stiffness of these paths in the presence of input noise.

Linear Interpolation. The path $\mathbf{X}_{\text{lin}}(t)$ is Lipschitz continuous (C^0) but its derivative is piecewise constant with discontinuities at the knots t_k . Adaptive solvers must restart the integration at each discontinuity (Morrill et al., 2022). Moreover, the step size within an interval is constrained by the magnitude of the slope. The total integration cost scales with the Total Variation of the sequence:

$$\text{NFE}_{\text{lin}} \propto \sum_{k=1}^{N-1} \|\mathbf{x}_{k+1} - \mathbf{x}_k\|. \quad (9)$$

Crucially, for a fixed sampling interval Δt , if the signal contains additive noise $\epsilon \sim \mathcal{N}(0, \sigma^2)$, the term $\|\mathbf{x}_{k+1} - \mathbf{x}_k\|$ does not vanish but is dominated by the noise amplitude. Thus, NFE_{lin} remains high regardless of the underlying signal smoothness.

Natural Cubic Splines. The path $\mathbf{X}_{\text{cub}}(t)$ is C^2 continuous. However, the interpolation condition $\mathbf{X}(t_k) = \mathbf{x}_k$ forces the spline to traverse the exact geometry of the noise (Wahba, 1990). The stiffness is dominated by the second derivative, which approximates the discrete second-order finite difference:

$$\left\| \frac{d^2 \mathbf{X}_{\text{cub}}(t)}{dt^2} \right\| \approx \frac{\|\mathbf{x}_{k+1} - 2\mathbf{x}_k + \mathbf{x}_{k-1}\|}{(\Delta t)^2}. \quad (10)$$

Substituting this into the complexity bound yields:

$$\text{NFE}_{\text{cub}} \propto \frac{1}{\Delta t} \sum_{k=2}^{N-1} \|\mathbf{x}_{k+1} - 2\mathbf{x}_k + \mathbf{x}_{k-1}\|. \quad (11)$$

This result indicates that cubic splines are extremely sensitive to high-frequency noise, as the cost scales with the local variance normalized by Δt .

A.3. Regularity of Smoothing Priors

We contrast the deterministic approach with our proposed Kernel and GP smoothing methods. Let $\mathbf{X}_h(t)$ denote the trajectory obtained via convolution with a smoothing kernel $K_h(t) = \frac{1}{h} K(\frac{t}{h})$ (Wand & Jones, 1995; Tsybakov, 2008).

Theorem (3.2). [Derivative Bounds for Smoothing Kernels] Let $\mathbf{X}_h(t)$ be constructed via Nadaraya-Watson regression (Cai, 2001) or as the posterior mean of a Gaussian Process with a stationary RBF kernel with lengthscale h (Rasmussen & Williams, 2006). The p -th derivative of the trajectory satisfies the following uniform bound:

$$\sup_{t \in [0, T]} \left\| \frac{d^p \mathbf{X}_h(t)}{dt^p} \right\| \leq \frac{C_p}{h^p} \|\mathbf{X}\|_\infty, \quad (12)$$

where $C_p = \int |K^{(p)}(u)| du$ is a constant depending solely on the kernel shape, and $\|\mathbf{X}\|_\infty$ is the bound on the input observations.

Proof. Both Kernel Smoothing and the GP posterior mean with RBF kernel can be expressed as linear operations on the kernel functions $k_h(t, \cdot)$. Since differentiation is a linear operator and commutes with the integral, we have $\frac{d^p}{dt^p} K_h(t) = h^{-p} K^{(p)}(t/h)$ (Wand & Jones, 1995). The bound follows immediately from the properties of the Gaussian kernel, where all derivatives are bounded and scale inversely with the bandwidth h . \square

Corollary (3.3). [Smoothing NFE Complexity] Substituting the bound from Theorem 3.2 into the NFE integral (Theorem 3.1) with $p+1$:

$$\text{NFE}(\mathbf{X}_h) \propto \int_0^T \left(h^{-(p+1)} \right)^{\frac{1}{p+1}} dt \propto h^{-1}. \quad (13)$$

This confirms that the solver complexity is controlled directly by the hyperparameter h . Unlike deterministic splines, the NFE for smoothing priors does not depend on the input noise variance or the sampling grid Δt , but only on the chosen spectral filter width h .

A.4. Complexity of Parallel Multi-Head Integration

We analyze the Multi-View architecture (MV-CDE and MVC-CDE), where the global state $\mathbf{Z}(t) = [\mathbf{z}^{(1)}(t), \dots, \mathbf{z}^{(M)}(t)]^\top$ involves M parallel latent trajectories. Each head m is driven by a control path $\mathbf{X}^{(m)}$ with a specific lengthscale h_m .

Theorem (3.4). [Parallel Integration Bottleneck] Consider an adaptive ODE solver integrating the block-diagonal system $\mathbf{Z}(t)$ with a global error tolerance δ . The total NFE is strictly governed by the minimum smoothing parameter in the ensemble:

$$\text{NFE}_{\text{total}} \propto \left(\min_{m=1}^M h_m \right)^{-1}. \quad (14)$$

Proof. Standard adaptive solvers (e.g., `dopri5` in `torchdiffeq`) control the error using a unified norm on the concatenated state vector. Let $\mathbf{e}_i \in \mathbb{R}^{\sum d_m}$ be the estimated local error vector at step i , composed of sub-vectors $\mathbf{e}_i^{(m)}$ for each head (Hairer et al., 1993). The step acceptance criterion is $\|\mathbf{e}_i\| \leq \delta$. Using the infinity norm (or broadly any p -norm for finite dimensions), this condition implies that the error in *every* component must satisfy the tolerance:

$$\forall m \in \{1, \dots, M\} : \quad \|\mathbf{e}_i^{(m)}\| \lesssim \delta. \quad (15)$$

From Theorem 3.1 and Theorem 3.2, the error estimate for the m -th head scales as:

$$\|\mathbf{e}_i^{(m)}\| \approx C \cdot \eta_i^{p+1} \cdot h_m^{-(p+1)}. \quad (16)$$

To ensure $\|\mathbf{e}_i^{(m)}\| \leq \delta$ for all m simultaneously, the global step size η_i must satisfy the tightest constraint:

$$\eta_i \leq \min_{m=1}^M \left(\frac{\delta}{C} \cdot h_m^{p+1} \right)^{\frac{1}{p+1}} \propto \min_{m=1}^M h_m. \quad (17)$$

The global step size is therefore limited by the trajectory with the highest stiffness, which corresponds to the smallest lengthscale $h_{\min} = \min_m h_m$. The total computational cost is:

$$\text{NFE} \propto \int_0^T \frac{1}{\eta(t)} dt \propto (h_{\min})^{-1}. \quad (18)$$

Thus, the computational efficiency of the MV-CDE and MVC-CDE models is bottlenecked by the finest temporal scale represented in the multi-view ensemble. \square

A.5. Explicit Error Comparison

To strictly quantify the performance gap, we evaluate the Mean Squared Error (MSE) of the estimator $\hat{\mathbf{X}}(t)$ with respect to the true latent process $\mathbf{X}(t)$. Since both Gaussian Process regression and Nadaraya-Watson (Kernel) smoothing are linear smoothers, they can be written as $\hat{\mathbf{X}}(t) = \mathbf{w}(t)^\top \mathbf{x}$, where $\mathbf{w}(t)$ is a weight vector.

Gaussian Process Error. The GP weights $\mathbf{w}_{\text{GP}} = (\mathbf{K} + \sigma^2 \mathbf{I})^{-1} \mathbf{k}(t)$ are derived analytically by solving the optimization problem $\min_{\mathbf{w}} \mathbb{E}[\|\mathbf{X}(t) - \mathbf{w}^\top \mathbf{x}\|^2]$. The resulting minimum error variance is:

$$\mathcal{E}_{\text{GP}}(t) = k(t, t) - \mathbf{k}(t)^\top (\mathbf{K} + \sigma^2 \mathbf{I})^{-1} \mathbf{k}(t). \quad (19)$$

This expression represents the theoretical lower bound on the reconstruction error for any linear estimator under the assumed prior (Rasmussen & Williams, 2006).

Kernel Smoothing Error. The Nadaraya-Watson weights are heuristic: $\mathbf{w}_{\text{NW}} = \mathbf{k}(t) / (\mathbf{k}(t)^\top \mathbf{1})$. The error for this sub-optimal weight selection is strictly larger:

$$\mathcal{E}_{\text{NW}}(t) = \mathcal{E}_{\text{GP}}(t) + \underbrace{(\mathbf{w}_{\text{NW}} - \mathbf{w}_{\text{GP}})^\top (\mathbf{K} + \sigma^2 \mathbf{I}) (\mathbf{w}_{\text{NW}} - \mathbf{w}_{\text{GP}})}_{\text{Excess Error} > 0}. \quad (20)$$

The Excess Error term is a quadratic form with a positive-definite matrix, meaning $\mathcal{E}_{\text{NW}}(t) > \mathcal{E}_{\text{GP}}(t)$ everywhere, except in trivial cases. This mathematically confirms that for a fixed smoothing bandwidth h , the GP provides a strictly more accurate reconstruction of the control path.

B. Experiments Setup

In this section, we detail the experimental setup used to evaluate the proposed MV-CDE and MVC-CDE architectures. Our evaluation focuses on the robustness of path-construction methods, their impact on the numerical efficiency of the ODE solver, and the resulting classification performance compared to baselines.

B.1. Datasets

We selected three multivariate time series classification benchmarks from the UEA (Bagnall et al., 2018) and UCR (Dau et al., 2019) repositories. These datasets exhibit diverse characteristics in terms of sequence length, dimensionality, and signal regularity.

CharacterTrajectories. This dataset consists of 2,858 sequences recording the trajectory of a pen tip during handwriting (3 features: x, y -coordinates, pen tip force). The maximum sequence length is 182 time steps. The task is to classify inputs into 20 distinct characters.

SpokenArabicDigits. This dataset comprises 8,800 time series representing MFCCs extracted from spoken Arabic digits. It features high dimensionality (13 features) and highly variable sequence lengths (ranging from 4 to 93 frames). The task is a 10-class digit classification.

UWaveGestureLibrary. This dataset contains 4,480 sequences of accelerometer gesture data (3 continuous spatial dimensions: x, y, z). The sequence length is fixed at 315 time steps, and the objective is to distinguish between 8 gesture patterns.

B.2. Data Preprocessing

To ensure rigorous evaluation and reproducibility, we employed a standardized preprocessing pipeline across all experiments. We partitioned each dataset into training (60%), validation (20%), and testing (20%) sets. All reported results are averaged over five independent random seeds.

Channel-wise Z-score normalization was applied using statistics computed solely on the training split to prevent data leakage. To accommodate variable-length sequences within batched continuous-time operations, we padded inputs to the maximum sequence length using the final observation value (rectilinear padding). This strategy yields a zero derivative ($dX/dt = 0$) in padded regions, allowing the adaptive solver to traverse them efficiently. The input features remain purely spatial ($x_t \in \mathbb{R}^d$), and the time domain is defined as regular intervals $t \in \{0, 1, \dots, T\}$ with $\Delta t = 1$.

B.3. Implementation Details and General Setup

All models were implemented in PyTorch and trained on a single NVIDIA L40 GPU using the Adam optimizer to minimize Cross-Entropy loss. The best models were selected based on validation accuracy checkpointing.

To ensure a fair computational comparison, the vector field f_θ for all ODE-based variants was parameterized by a Multilayer Perceptron (MLP) with a single hidden layer of 128 units and tanh activations. Furthermore, all models utilize a consistent hidden dimension of 128 units throughout their architectures. We used the `dopri5` adaptive solver.

To quantify performance and efficiency, we utilize the following metrics:

- **Total wall-clock time** is calculated as the sum of: (i) trajectory fit time, (ii) training duration, and (iii) the final test evaluation pass.
- **Average NFE per batch** is reported during the test phase to assess solver efficiency. This metric reflects the numerical complexity of integrating the stiffest trajectory within a batch.

B.4. Baselines and Hyperparameter Optimization

Non-CDE Baselines (ODE-RNN, GRU-D). We compare our methods against standard recurrent architectures capable of modeling continuous dynamics.

- **ODE-RNN (Rubanova et al., 2019):** The output layer of the ODE function is initialized with zeros ($dh/dt \approx 0$ initially) for stability.
- **GRU-D (Che et al., 2016):** The decay layer weights are initialized to zero ($\gamma = 1$ initially) to prevent signal vanishing at the start of training.

Unlike our proposed methods, these baselines required distinct hyperparameter tuning to achieve convergence. We optimized the learning rate (e.g., searching within $\{10^{-3}, 5 \cdot 10^{-3}, 10^{-2}\}$) and solver tolerance ($\{10^{-2}, 10^{-3}\}$) specifically for each dataset. For instance, ODE-RNN required a learning rate of 0.01 on SpokenArabicDigits and 0.005 on CharacterTrajectories to match the best performance.

Log-Neural CDE. This baseline (Walker et al., 2024) interpolates Log-Signatures computed over fixed time windows. Similar to the non-CDE baselines, we found that this model required higher learning rates than standard NCDEs. We optimized the window step size from $\{3, 5, 10, 20, 30\}$, Log-Signature depth $\{1, 2\}$, and the learning rate ($\{5 \cdot 10^{-3}, 10^{-2}\}$).

Standard Neural CDEs (Linear & Cubic). (Kidger et al., 2020) These models use fixed paths constructed via Linear Interpolation or Natural Cubic Splines. Crucially, to strictly evaluate the impact of path construction, these models utilized the exact same optimization schedule and learning rates as our proposed methods (detailed in Section B.6).

B.5. Proposed Methods

Kernel CDE & GP CDE. These models employ smooth path construction using Nadaraya-Watson kernel smoothing or Gaussian Process posterior means to generate a single continuous trajectory per sample. Unlike the multi-view methods, these do not utilize attention mechanisms. We evaluated GP observation noise across $\sigma \in \{0.01, 0.05\}$.

MV-CDE & MVC-CDE. These are the core contributions of this work, where $M \geq 1$ trajectories are constructed dynamically.

- **MV-CDE:** Uses M learnable query vectors $q_m \sim \mathcal{N}(0, 1)$ to compute attention weights and construct M smooth trajectories via weighted interpolation.
- **MVC-CDE:** Incorporates a feature extraction stage (2-layer 1D CNN, kernel size 3, 128 hidden units) before attention computation. The attention weights are derived from latent features, while the continuous path interpolates the original input space.

Global Smoothing Strategy. For all smoothing-based models, we swept over raw bandwidth factors in the range $[0.01, 9.0]$. The effective smoothing scale is adapted to the sequence length, such that $h_{\text{eff}} = h_{\text{raw}} \times T_{\text{max}}$.

B.6. Dataset-Specific Optimization Settings

The following settings were applied uniformly to Linear, Cubic, and our proposed models. As noted in Section B.4, other baselines relied on separately optimized parameters.

- **CharacterTrajectories:** Batch size 256, learning rate 10^{-4} , weight decay 10^{-5} , 25 epochs. Solver tolerance 10^{-3} .
- **SpokenArabicDigits:** Batch size 2048, learning rate 10^{-3} , weight decay 10^{-4} , 13 epochs. Solver tolerance 10^{-3} .
- **UWaveGestureLibrary:** Batch size 512, learning rate 10^{-3} , weight decay 10^{-5} , 30 epochs. Solver tolerance 10^{-4} .

B.7. Ablation Studies and Visualization

Solver Tolerance Analysis. To investigate speed-accuracy trade-offs specifically for spline-based methods, we conducted ablation studies on the solver tolerance for the Linear and Cubic Neural CDE baselines. We varied the absolute and relative tolerances across $\{10^{-1}, 10^{-2}, 10^{-3}, 10^{-4}\}$ to determine whether relaxing precision constraints could accelerate these models without catastrophic accuracy loss. This results is shown in Figures 7, 8, and 9.

Impact of Head Count and Smoothing. We conducted comprehensive ablation studies varying the number of attention heads $M \in [1, 8]$. We tested two smoothing configurations: (1) *homogeneous*, where the bandwidth h is identical across all heads; and (2) *heterogeneous*, where h is distinct for each head (initialized with geometrically spaced values). This comparison, visualized in Figure 6, assesses the solver’s ability to integrate systems with multiscale stiffness.

Noise Robustness Analysis. To evaluate the stability of path-construction mechanisms under perturbation, we subject the best-performing models to a robustness test. We inject additive white Gaussian noise $\xi \sim \mathcal{N}(0, \lambda^2 I)$ into the test set features, sweeping the noise level λ across a range of intensities. We monitor both the degradation in test accuracy and the variation in the Average NFE. This experiment is designed to verify the hypothesis that smoothing-based methods (Kernel, GP) maintain efficient solver dynamics by filtering high-frequency jitter, whereas direct interpolation methods (Linear, Cubic) transmit noise directly into the vector field, forcing the adaptive solver to take excessive steps to track the irregularities.

Attention Visualization. We explicitly extracted the attention weights from trained MV-CDE and MVC-CDE models. This enables a qualitative analysis of temporal feature selection, verifying whether the multi-head mechanism effectively focuses on informative trajectory segments while suppressing noise.

C. Extended Experimental Results and Implementation Details

In this section, we provide supplementary experimental analysis to support the claims made in the main text. Specifically, we analyze the limitations of single-kernel baselines, investigate the impact of smoothing initialization strategies on the accuracy-efficiency trade-off, and provide a granular breakdown of computational costs.

C.1. Full Experimental Results

The Table 1 presents the comprehensive comparison of all evaluated models, including precise hyperparameters used to achieve the reported results.

Table 1. Performance comparison of various models across CharacterTrajectories, SpokenArabicDigits, and UWaveGestureLibrary datasets. Our proposed methods are marked with (Ours), with MVC GP being our primary architecture. Best results in each category are highlighted in **bold** (for NFE, the best non-zero value is highlighted).

Model	Test Acc. (%)	Total Time (s)	Avg NFE	Hyperparameters
CharacterTrajectories				
Linear	85.63 \pm 1.90	118.79 \pm 3.06	633.11 \pm 28.31	LR:0.0001 — Tol:0.001
Cubic	86.61 \pm 0.86	132.26 \pm 3.46	595.91 \pm 9.99	LR:0.0001 — Tol:0.001
ODE-RNN	74.65 \pm 4.07	333.62 \pm 23.88	1953.03 \pm 317.93	LR:0.005 — Tol:0.001
GRU-D	93.17 \pm 0.78	10.56 \pm 0.39	0.00 \pm 0.00	LR:0.005 — Tol:0.001
Log-NCDE	90.87 \pm 0.89	163.57 \pm 1.96	839.86 \pm 26.51	LR:0.005 — Tol:0.001 — Depth:1.0 — Step:10.0
Gaussian (Ours)	89.20 \pm 2.26	49.53 \pm 2.24	165.63 \pm 4.23	BW:5.95 — LR:0.0001 — Tol:0.001
GP (Ours)	88.15 \pm 0.42	46.41 \pm 1.61	169.23 \pm 2.06	LR:0.0001 — Tol:0.001 — LS:71.4 — Noise:0.01
MV Gaussian (Ours)	89.93 \pm 0.73	50.31 \pm 2.78	190.49 \pm 10.77	BW:[3.57,11.9,47.6,166.6] — LR:0.0001 — Tol:0.001
MV GP (Ours)	92.97 \pm 1.74	46.20 \pm 1.65	206.60 \pm 5.60	BW:[3.57,11.9,47.6,166.6] — LR:0.0001 — Tol:0.001 — Noise:0.01
MVC Gaussian (Ours)	91.71 \pm 1.40	51.65 \pm 1.63	209.34 \pm 15.26	BW:[3.57,11.9,47.6,166.6] — LR:0.0001 — Tol:0.001 — KS:3.0
MVC GP (Ours, Main)	95.07 \pm 0.49	22.63 \pm 0.48	95.17 \pm 7.41	BW:[166.6,166.6,166.6,166.6] — LR:0.0001 — Tol:0.001 — Noise:0.01 — KS:3.0
SpokenArabicDigits				
Linear	86.09 \pm 1.28	106.15 \pm 3.76	2237.40 \pm 20.02	LR:0.001 — Tol:0.001
Cubic	84.93 \pm 2.10	57.90 \pm 1.73	1003.80 \pm 24.19	LR:0.001 — Tol:0.001
ODE-RNN	68.47 \pm 2.62	53.29 \pm 4.81	1359.20 \pm 170.47	LR:0.01 — Tol:0.001
GRU-D	96.57 \pm 0.13	2.02 \pm 0.09	0.00 \pm 0.00	LR:0.01 — Tol:0.001
Log-NCDE	86.81 \pm 0.54	11.32 \pm 0.16	215.80 \pm 9.23	LR:0.01 — Tol:0.001 — Depth:1.0 — Step:20.0
Gaussian (Ours)	96.32 \pm 0.61	14.27 \pm 0.58	187.00 \pm 5.10	BW:3.25 — LR:0.001 — Tol:0.001
GP (Ours)	96.12 \pm 0.33	11.73 \pm 0.46	181.40 \pm 5.37	LR:0.001 — Tol:0.001 — LS:39.0 — Noise:0.01
MV Gaussian (Ours)	97.11 \pm 0.27	19.59 \pm 0.68	195.40 \pm 6.54	BW:[1.95,6.5,26,0.91,0] — LR:0.001 — Tol:0.001
MV GP (Ours)	97.52 \pm 0.39	13.61 \pm 0.48	187.00 \pm 7.21	BW:[6.5,26,0.91,0] — LR:0.001 — Tol:0.001 — Noise:0.01
MVC Gaussian (Ours)	97.34 \pm 0.46	19.12 \pm 0.56	191.40 \pm 9.94	BW:[1.95,6.5,26,0.91,0] — LR:0.001 — Tol:0.001 — KS:3.0
MVC GP (Ours, Main)	98.28 \pm 0.29	7.32 \pm 0.15	95.40 \pm 0.89	BW:[91.0,91.0,91.0] — LR:0.001 — Tol:0.001 — Noise:0.01 — KS:3.0
UWaveGestureLibrary				
Linear	83.86 \pm 1.87	176.19 \pm 5.13	4340.60 \pm 216.07	LR:0.001 — Tol:0.0001
Cubic	84.77 \pm 2.62	53.22 \pm 2.25	1076.60 \pm 33.57	LR:0.001 — Tol:0.001
ODE-RNN	37.95 \pm 2.06	205.21 \pm 1.27	4397.20 \pm 2.68	LR:0.005 — Tol:0.01
GRU-D	78.86 \pm 2.62	5.74 \pm 0.11	0.00 \pm 0.00	LR:0.01 — Tol:0.001
Log-NCDE	70.91 \pm 6.36	34.87 \pm 0.53	753.80 \pm 25.60	LR:0.01 — Tol:0.001 — Depth:1.0 — Step:30.0
Gaussian (Ours)	88.41 \pm 2.59	14.84 \pm 0.80	236.60 \pm 6.84	BW:15.75 — LR:0.001 — Tol:0.0001
GP (Ours)	91.14 \pm 1.87	8.69 \pm 0.25	170.60 \pm 5.37	LR:0.001 — Tol:0.0001 — LS:441.0 — Noise:0.05
MV Gaussian (Ours)	89.77 \pm 3.31	17.97 \pm 1.79	320.60 \pm 23.08	BW:[9.45,31.5,126.0,441.0] — LR:0.001 — Tol:0.0001
MV GP (Ours)	92.95 \pm 1.24	17.19 \pm 1.20	359.00 \pm 23.62	BW:[15.75,63.0,189.0] — LR:0.001 — Tol:0.0001 — Noise:0.05
MVC Gaussian (Ours)	90.00 \pm 2.03	19.87 \pm 1.78	453.80 \pm 38.28	BW:[15.75,15.75,15.75,15.75] — LR:0.001 — Tol:0.0001 — KS:3.0
MVC GP (Ours, Main)	95.39 \pm 0.28	12.29 \pm 0.27	218.60 \pm 10.04	BW:[31.5,63.0,126.0] — LR:0.001 — Tol:0.0001 — Noise:0.05 — KS:3.0

C.2. Single-Kernel Smoothing Baselines

To verify that the performance gains stem from the Multi-View Attention mechanism rather than from the use of Gaussian Processes alone, we evaluated single-trajectory models without attention.

Figure 7 presents the performance landscape (Error Rate vs. Training Time) for single-kernel methods compared to standard baselines. While single-kernel models often outperform ODE-RNN in speed, they exhibit high variance in accuracy across different bandwidth choices. This instability underscores the necessity of the Multi-View mechanism to robustly aggregate dynamics.

C.3. Impact of Bandwidth Initialization Strategy

We further investigate how the diversity of smoothing scales impacts the model’s position on the Pareto frontier. We compare two initialization configurations:

- **Heterogeneous Smoothing (Figure 8):** Bandwidths are initialized with geometrically spaced values to capture multi-scale dynamics.

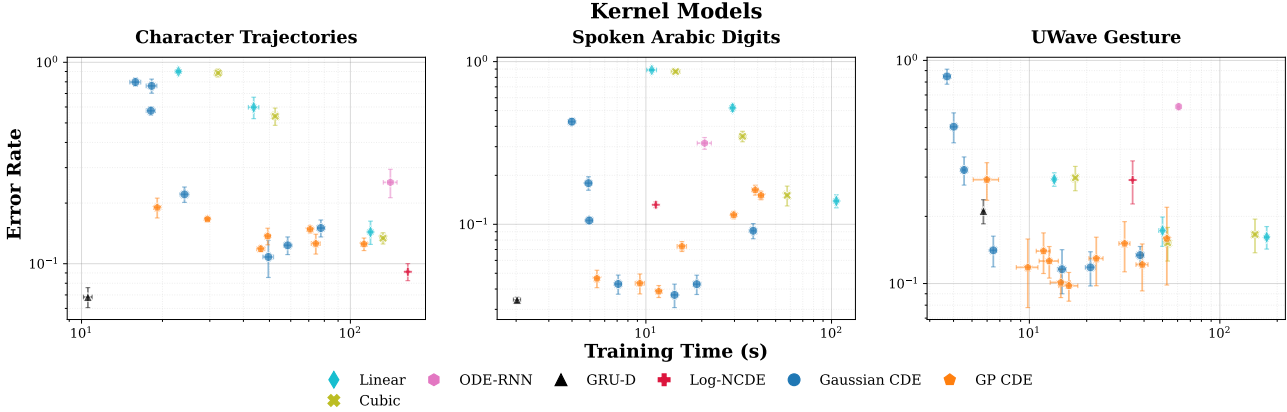


Figure 7. Single-Kernel Smoothing Performance. The scatter plots illustrate the trade-off between error rate and training time for single-kernel Gaussian and GP models.

- **Homogeneous Smoothing (Figure 9):** All heads share the same initial bandwidth.

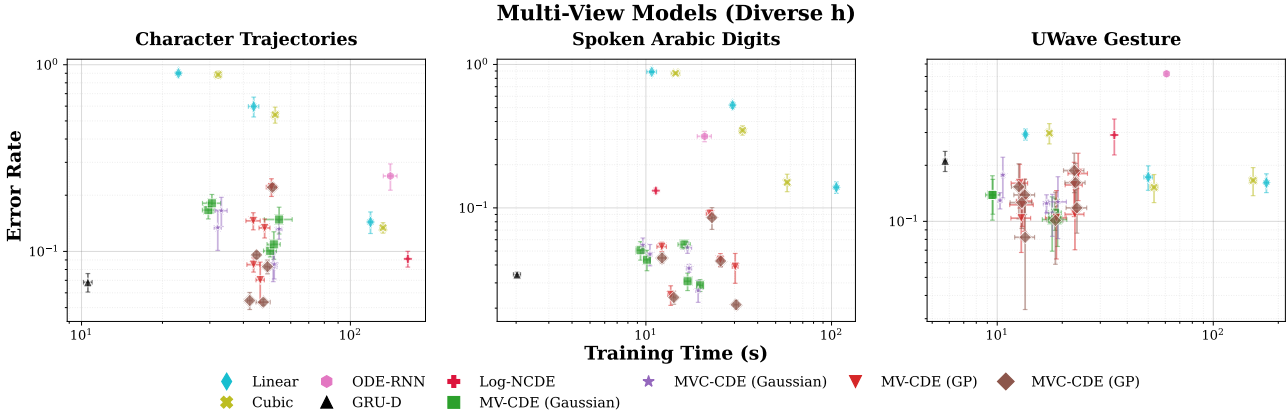


Figure 8. Pareto Efficiency: Heterogeneous Bandwidths. Error Rate vs. Training Time comparison when attention heads are initialized with diverse smoothing scales.

Analysis. As shown in Figure 8, the Heterogeneous strategy pushes the proposed models (MVC-GP and MVC-Gaussian) towards the bottom-left corner of the plot, indicating superior accuracy with minimal training time. This diversity enables the model to effectively disentangle stiff and smooth dynamics. In contrast, while the Homogeneous setting (Figure 9) still outperforms standard Linear and Cubic baselines, the lack of scale diversity results in a less favorable trade-off, with models often clustering at higher error rates or longer training times than their heterogeneous counterparts.

C.4. Detailed Computational Cost Analysis

To explain the speedups reported in the main text, Figure 10 provides a granular breakdown of the wall-clock time. We distinguish between:

1. **Pure Training Time:** The time spent by the ODE solver during the iterative training loop.
2. **Overhead:** The combined time for Trajectory Fitting (pre-computation) and Inference (which includes CDE integration).

Breakdown. Standard NCDEs suffer from high training latency due to the stiffness of the control paths. In contrast, our smoothing-based methods incur a one-time pre-computation cost but drastically reduce the pure training time. This shift of complexity from the iterative loop to pre-processing results in a significantly lower total time to convergence.

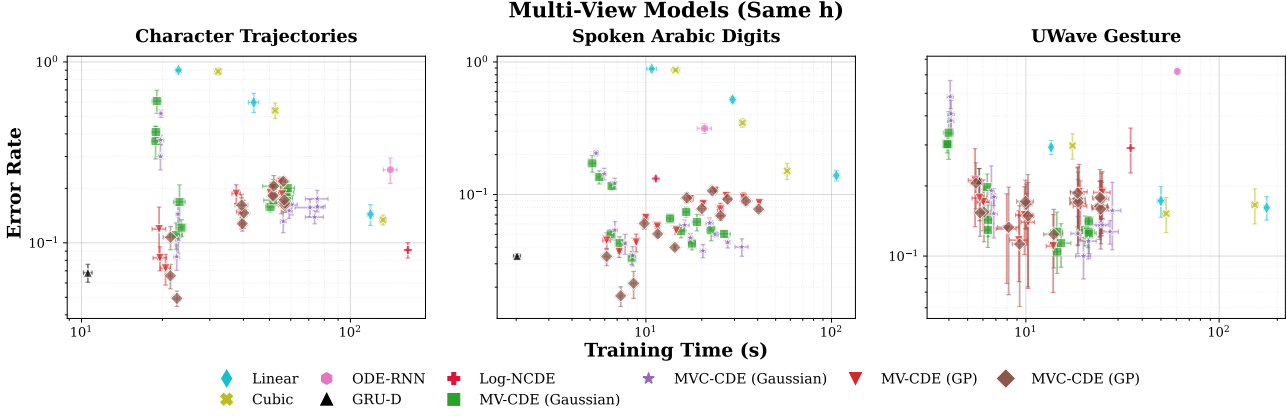


Figure 9. **Pareto Efficiency: Homogeneous Bandwidths.** Performance landscape when all attention heads are initialized with identical smoothing scales.

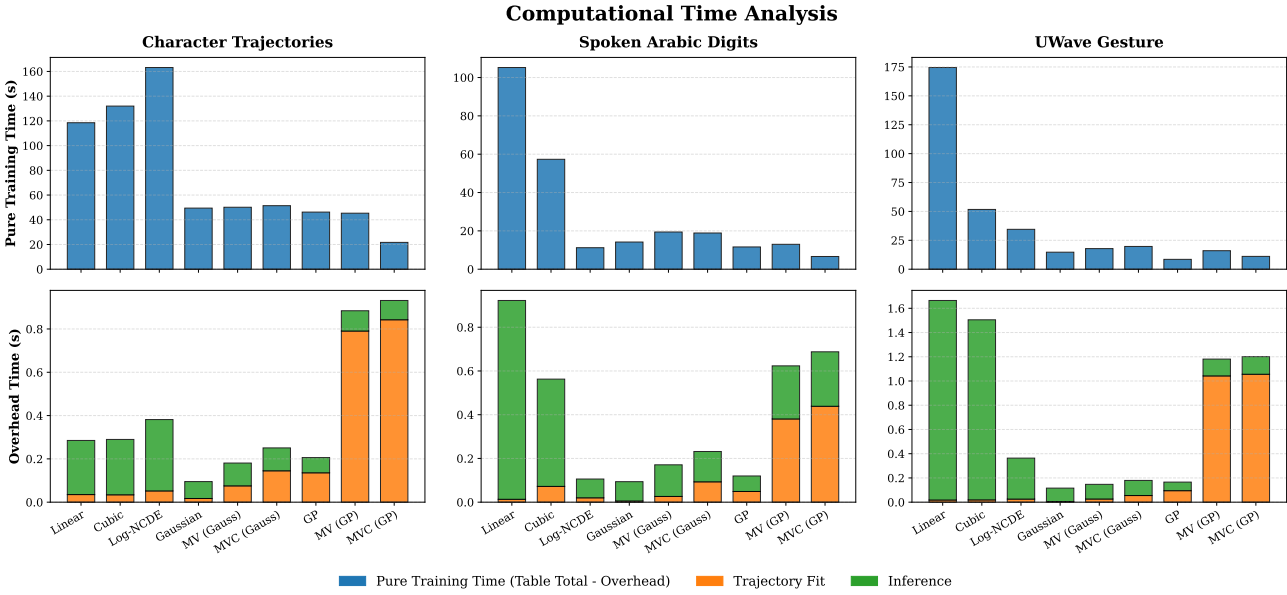


Figure 10. **Computational Cost Breakdown.** Top: Pure training time significantly decreases for smoothing-based models compared to standard Linear and Cubic baselines, as the smoother paths reduce solver stiffness. Bottom: The overhead analysis shows that our method incurs a one-time trajectory-fitting cost (orange segments), which is outweighed by the substantial reduction in iterative training time.